

Article

Influence of Milling Time and Ball-to-Powder Ratio on Mechanical Behavior of FeMn₃₀Cu₅ Biodegradable Alloys Prepared by Mechanical Alloying and Hot-Forging

Subbarayan Sivasankaran ¹, Hany R. Ammar ^{1,*}, Bandar Almangour ^{2,3}, Samir Ali Elboroloso ^{4,5}, Abdel-baset H. Mekky ⁶ and Abdulaziz S. Alaboodi ¹

- ¹ Department of Mechanical Engineering, College of Engineering, Qassim University, Buraydah 51452, Saudi Arabia
- ² Department of Mechanical Engineering, King Fahd University of Petroleum & Minerals, Dhahran 31261, Saudi Arabia
- ³ Interdisciplinary Research Center for Intelligent Manufacturing & Robotics, King Fahd University of Petroleum & Minerals, Dhahran 31261, Saudi Arabia
- ⁴ Maxillofacial Surgery and Diagnostic Sciences Department, College of Dentistry, Qassim University, Buraydah 52571, Saudi Arabia
- ⁵ Oral and Maxillofacial Surgery Department, Faculty of Dentistry, Beni-Suef University, Beni-Suef 62511, Egypt
- ⁶ Department of Physics, College of Science and Arts El-Meznab, Qassim University, Buraydah 51931, Saudi Arabia
- * Correspondence: hanyammar@qec.edu.sa



Citation: Sivasankaran, S.; Ammar, H.R.; Almangour, B.; Elboroloso, S.A.; Mekky, A.-b.H.; Alaboodi, A.S. Influence of Milling Time and Ball-to-Powder Ratio on Mechanical Behavior of FeMn₃₀Cu₅ Biodegradable Alloys Prepared by Mechanical Alloying and Hot-Forging. *Crystals* **2022**, *12*, 1777. <https://doi.org/10.3390/cryst12121777>

Academic Editor: Shouxun Ji

Received: 1 November 2022

Accepted: 5 December 2022

Published: 7 December 2022

Publisher's Note: MDPI stays neutral with regard to jurisdictional claims in published maps and institutional affiliations.



Copyright: © 2022 by the authors. Licensee MDPI, Basel, Switzerland. This article is an open access article distributed under the terms and conditions of the Creative Commons Attribution (CC BY) license (<https://creativecommons.org/licenses/by/4.0/>).

Abstract: FeMn₃₀Cu₅ is a biodegradable and multi-component alloy that can be used to repair bone defects in load-bearing parts in the medical field. This work focuses on studying the influence of milling time and ball-to-powder ratio (BPR) on the mechanical behavior of FeMn₃₀Cu₅ alloys via mechanical alloying and hot-forging. Three different milling times (1, 5.5, and 10 h) and BPRs (5:1, 10:1, and 15:1) were used as the main independent variables. MA was performed at 300 rpm in ethanol; the synthesized powders were dried, hot-compacted at 550 MPa, and sintered under an inert atmosphere (1000 °C, 15 min) using a medium-frequency induction furnace and hot-forging. The mechanical behavior in terms of Vickers hardness, compressive stress–strain curves, and percentage theoretical density was investigated. This experimental work revealed that both milling time and BPR significantly influenced the grain size reduction owing to variations in the severe plastic deformation and mechanical collisions produced by the milling medium. The hardness and ultimate strength of the FeMn₃₀Cu₅ alloy processed at 10 h and 15:1 BPR were 1788.17 ± 4.9 MPa, which was 1.5 times higher than those of the same alloy processed at 1 h and 5:1 BPR (1200.45 ± 6.5 MPa). Austenite iron (g-Fe), ferrite-iron (a-Fe), a-Mn, and a-Cu phases were observed in XRD and SEM images. The formed a-Mn and a-Cu overlapped with the g-Fe lattice because of the diffusion of Mn and Cu atoms during sintering and hot-forging. The incorporated 30 wt.% of Mn and 5 wt.% of Cu stabilize the austenite phase (good for MRI scans in medical applications), which contributed to promoting superior mechanical properties with milling time (10 h) and BPR (15:1) due to severe structural defects.

Keywords: Fe-Mn-Cu alloys; mechanical alloying; hot-forging; characterization; mechanical behavior

1. Introduction

Currently, biodegradable alloys with controlled corrosion rates in a tissue environment are typically produced from iron-based alloys rather than magnesium-based alloys [1–4]. Biocompatible parts perform their function over a period of time and begin to degrade safely inside organs without any side effects [5–7]. Iron-, magnesium-, and zinc-based alloys are commonly used biodegradable alloys that are tested in animals (orthopedic and cardiovascular parts) and require high structural strength [8–10]. Comparable mechanical and biocompatible properties can be achieved from Mg-based alloys [11–13]. Although

mg-based alloys exhibit a high corrosion rate in osteogenic environments, they produce hydrogen gas, which restricts their application in the medical field. Zn-based alloys are an alternative and new class of biodegradable metals that begin to corrode moderately [14–16]. According to several researchers and recommendations [17–21], iron-based alloys exhibit excellent biocompatibility. Moreover, Fe-based alloys exhibit high strength and ductility. However, the degradation rate of iron is insufficient to produce biocompatible parts [22–24]. Therefore, some studies have found that the incorporation of Mn with Fe significantly enhances the degradation rate of Fe [17,22–26]. In addition to Mn, Si, Pd, Ca, and Ag, C and Cu are alloying elements that increase the corrosion rate and improve the bioresorbability of implant parts [3,17,27,28].

Schinhammer et al. [17] investigated the use of FeMn with Pd as a biodegradable alloy. The authors found that the incorporation of Pd into the FeMn alloy promoted micro-galvanic corrosion by acting as a cathodic site. The incorporation of Ca and Mg into FeMn alloys was studied by Hong et al. [29], who developed the alloys via mechanical alloying. Their results demonstrated an improvement in corrosion rate and tensile strength. Zu et al. [30] investigated the use of Fe-Mn-Si alloys, which increase corrosion rate and ultimate tensile strength, owing to the formation of martensite and austenite phases after consolidation [30]. Liu et al. [31] developed an Fe-Mn-Ag alloy and conducted electrochemical tests, which demonstrated that the developed alloys possess a high corrosion rate, owing to the precipitation of Ag particles. Hufenbach et al. [32] developed an FeMn₃₀C₁ alloy with 0.025 wt.% of S, due to which the alloy exhibited MnS as precipitates. The formed MnS precipitates enhanced the strength and corrosion rate of simulated body fluid. Tang et al. [33] reported that the selection and incorporation of Cu in FeMn alloys boosted the antibacterial effect and reduced infections during medical treatments, especially in surgery. According to Zhang et al. [34], Cu is an important microelement in the human body that stabilizes the functions of human organs and regulates metabolic processes, as described by Ingle et al. [35]. Recently, Mandal et al. [35] demonstrated the improvement in the degradability and biocompatibility of FeMnCu alloys through *in vitro* and *in vivo* studies and recommended their use in fracture fixation elements. In summary, based on the literature, Cu can be used as an alloying element in FeMn systems, which can be further used as a biodegradable alloy. FeMn-based biodegradable alloys can be processed using vacuum arc melting [36] and power metallurgy [30] techniques, in which the P/M route can provide improved properties owing to the elimination of intermetallic compound formation. Mechanical alloying (MA) is the best processing method for the P/M route, which produces a homogeneous alloy [37]. MA is not only used for the reduction of powder particle size, crystallite size, and changes in the internal structures. The MA process significantly changes the powder surface morphology, deformation ability of powder particles, and produces meta stable phases [38]. In MA, several process parameters influence the performance of the developed alloy, among which milling time and ball-to-powder ratio (BPR) are significant parameters [39]. In general, an increase in BPR increases milling effects, such as the number of mechanical collisions over time, and lowers the powder particles, consequently increasing the velocity of a single ball during milling [40]. To the best of the authors' knowledge, there are no studies related to the variation of MA process parameters on the development of FeMn biodegradable alloys to examine the effect of grain size on structural changes, variation in hardness, percentage theoretical density, and mechanical performance. Therefore, the main objectives of the present study are to: design and develop an FeMn₃₀Cu₅ alloy via MA; vary the milling times (5.5, 10, and 15 h) and BPRs (5:1, 10:1, and 15:1); consolidate the synthesized powders into bulk samples through hot-compaction followed by sintering using a medium-frequency induction furnace and hot-forging; and examine the mechanical behavior in terms of relative density, hardness, and compressive stress–strain curves.

2. Materials and Methods

2.1. Materials Synthesis Using Different Milling Parameters

Pure elemental powders of Fe, Mn, and Cu (more than 99% in purity) were purchased from M/s Nanografi, Jena, Germany. Iron powders of 65 wt.%, manganese powders of 35 wt.%, and balance of Cu as 5 wt.% were weighed using electronic balance with four-digit resolution to develop FeMn30Cu5 biodegradable alloys with different processing parameters. Higher amounts of Mn (≥ 30 wt.%) content in Fe enhances the corrosion rate and compatibility with magnetic resonance imaging (MRI), which is important for biodegradable applications [41]. Cu is an important element for improving the metabolic function and stability of organs [34]. A high-energy planetary ball mill (Pulverisette 5/2 classic line; Fritsch GmbH, Idar-Oberstein, Germany) was used to conduct the experiments. The milling times (1, 5.5, and 10 h) and ball-to-powder mass ratios (BPRs, 5:1, 10:1, and 15:1) as the main input parameters were varied in this study. The milling parameters used in this study are listed in Table 1. Intermittent milling was carried out to eliminate the heat effect produced by the high-energy ball mill in which 15 min forward milling (clockwise rotation), 15 min pause, 15 min reverse milling (counterclockwise), and 15 min pause were programmed in the machine. Wet milling (ethanol) was performed automatically using a programmable control system.

Table 1. Milling parameters used in the present study.

Name of Alloy	Milling Time, h	Ball-to-Powder Mass Ratio	Other Milling Conditions
FeMn30Cu5	1, 5.5, and 10	5:1, 10:1, and 15:1	Wet milling—ethanol. Speed—300 rpm

2.2. Hot-Compaction, Sintering, and Hot-Forging

The synthesized powders were dried and stress relieved under vacuum in a tube furnace (M/s Nabatherm, Lilienthal, Germany) at a temperature of 120 °C for 30 min. The stress-relieved powders were then hot-compacted at a temperature of 550 °C for 45 min at a pressure of 550 MPa and held for 10 min. The stress-relieved powders were poured inside the die-sets, closed properly to avoid oxidization, and kept inside an electric induction furnace (M/s Nabatherm, Lilienthal, Germany). The heating cycles were programmed using Nabatherm software, and a heating rate of 10 °C per min was set. Once the required temperature was 550 °C, and the holding time was 45 min, the hot-die sets were safely removed and pressed at a pressure of 550 MPa using a 25-ton hydraulic press. H13 die-steel was used for the hot-compaction. Hot pellets 15 mm in diameter and 22 mm in height were obtained. A graphite lubricant was applied to the die-wall surface before pouring the powder.

The hot-compacted pellets were sintered in a medium frequency induction furnace (M/s Zhengzhou Yuanjie Chemical co., ltd, Zhengzhou, China). First, a hot-compacted pellet was placed inside a graphite crucible; second, a hot pellet with a graphite crucible was placed inside an alumina crucible that surrounded a copper tube coil with a cooling water connection, and a lid with a hole to purge the Ar gas connection was used. A heat input power of 2000 watts was used, which reached a temperature of 1000 ± 20 °C and was held for 10 min. The sintered pellet was kept inside an H13 pre-heated and graphite-coated die-set, forged at a pressure of 50 MPa, and cooled in air. Figure 1 shows a schematic representation of the crystal structure of the as-received raw elemental powders, MA process, and processing methods used in this study.

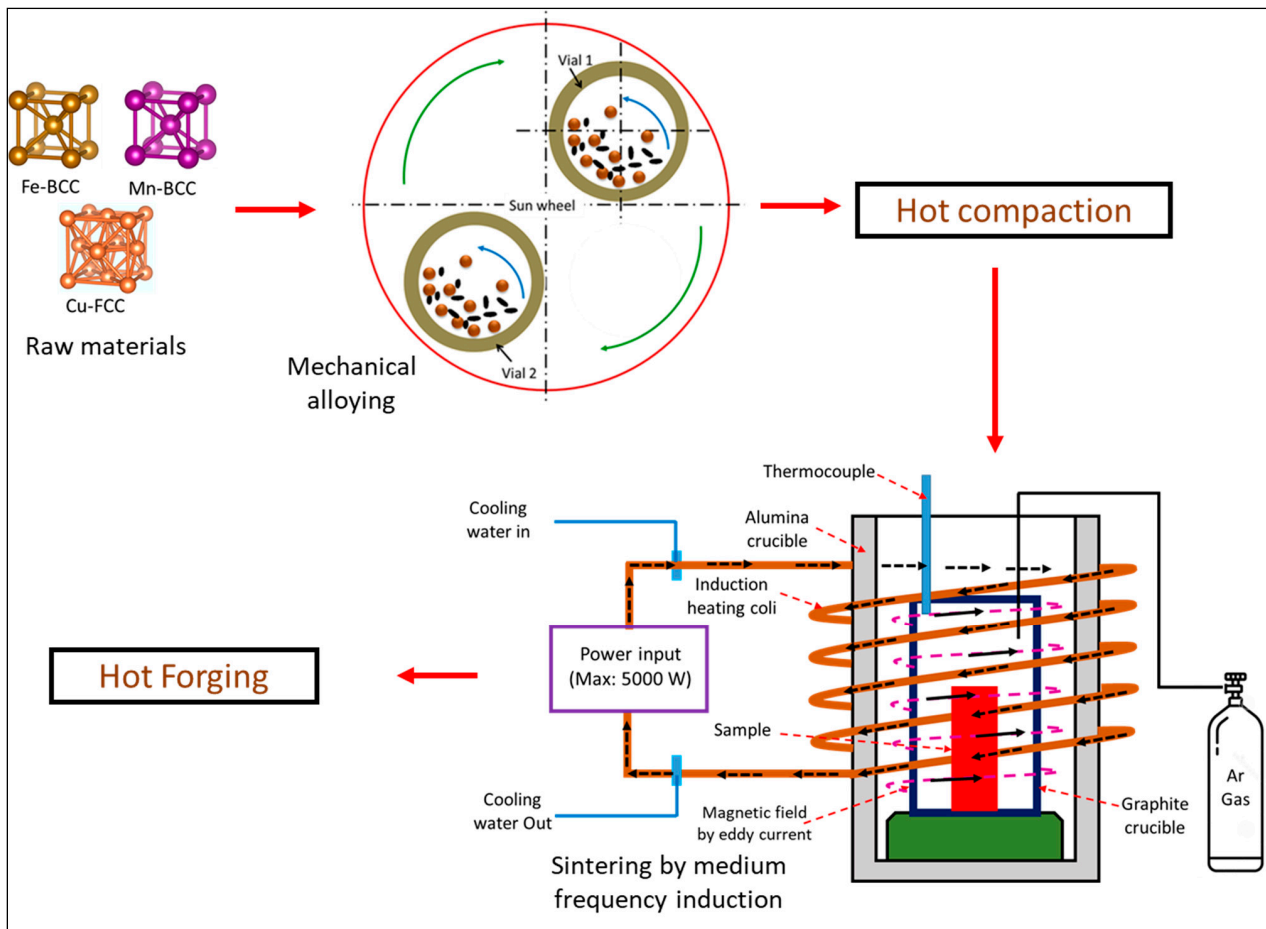


Figure 1. Schematic showing the elemental powders, mechanical alloying process, hot-compaction, sintering using medium frequency furnace, and hot-forging used in the present study.

2.3. Mechanical Testing and Characterization

The forged pellets were then sized to 14 mm in diameter and 18 mm in height for mechanical testing. Compression tests were conducted using a universal testing machine (M/s MTS Corporation, Eden Prairie, MN, USA) with a traverse speed of 1 mm/min. The machine was connected to a data acquisition system using Test-works software. Three trials were conducted for each sample, and the average was used for investigation. Data obtained from the machine (load and deformation) were used to determine the mechanical properties. The engineering compressive stress (σ_c) was calculated using Equation (1):

$$\sigma_c = \frac{F_c}{A} \quad (1)$$

where F_c is the compressive load acting on the specimen in 'N', and 'A' is the initial cross-sectional area of specimen in ' mm^2 '. The corresponding engineering strain (ϵ_c) was calculated using Equation (2):

$$\epsilon_c = \frac{\delta h}{h} \quad (2)$$

where δh is the change in height (i.e., deformation) in mm, and h is the initial height of the specimen. Compressive yield strength was calculated by 0.2% strain off-set method. The actual density of the forged samples (ρ_{act}) was measured using Archimedes principle, as per Equation (3):

$$\rho_{act} = R \times \rho_{water} \quad (3)$$

where R is the relative density, and ρ_{water} is the density of water at room temperature. The relative density (R) of the forged samples was determined using Equation (4):

$$R = \frac{m_{air}}{(m_{air} - m_{water})} \quad (4)$$

where m_{air} is the mass of the sample in the air column, and m_{water} is the mass of the sample in the water column. The percentage theoretical density (%TD) was calculated using Equation (5):

$$\%TD = \frac{\rho_{act}}{\rho_{th}} \times 100 \quad (5)$$

where ρ_{th} is the theoretical density, which was calculated based on the rule of mixtures, as per Equation (6):

$$\rho_{th} = f_{Fe}\rho_{Fe} + f_{Mn}\rho_{Mn} + f_{Cu}\rho_{Cu} \quad (6)$$

where f_{Fe} , f_{Mn} , and f_{Cu} are the volume fractions of Fe, Mn, and Cu, respectively. ρ_{Fe} , ρ_{Mn} , and ρ_{Cu} are the theoretical densities of Fe, Mn, and Cu, respectively. Bulk samples of 15 mm in diameter with a height of approximately 10 mm pellets were used to examine the Vickers hardness, phase formation using X-ray diffraction (XRD, Empyrean, Malvern Panalytical, source: CuK α = 1.54 Å), and microstructural evolutions by HR-SEM with EDS and EBSD analyses (Apreo FEG-HR-SEM, 30 keV, 1.3 nm resolution at 1 keV). Before HR-SEM analyses, hot-forged samples were mounted with acrylic resin using a mounting press (Cito-Press 30, Struers, Cleveland, OH, USA); mechanical grinding was carried out using different grit sizes of SiC papers (300, 400, 600, 800, 1000, 2000, and 3000 grits/inch²); polishing was carried out in 3 μ m diamond solution using a polishing machine (Labosystem, Struers, Cleveland, OH, USA); and then, the samples were chemically etched using Nital solution (3% HNO₃ in an ethanol solution). Differential scanning calorimetry (DSC) was performed on the synthesized powders using a Netzsch TG-DSC instrument up to 1600 °C at a heating rate of 10 °C per min. The DSC test was conducted under an Ar atmosphere to examine the displacement reaction upon heating. Micro-hardness with a load of 100 gf/mm² for 15 s was applied to the sample at room temperature, and at least 10 readings were recorded at different locations. Before conducting the hardness tests, the samples were ground with SiC grit papers of different grades (200, 400, 600, 1000 and 2000) and polished using an Al₂O₃ lapping paste. The hardness test indentation diagonal size (d) was measured, and the Vickers hardness number was calculated using Equation (7):

$$HV = 1.854 \frac{F}{d^2} \quad (7)$$

where F is the applied load in kgf. Averages, standard deviations, and standard errors were calculated.

3. Results and Discussion

3.1. Influence of Milling Time and BPR on Thermal and X-ray Diffraction Analyses

Figure 2 shows the DSC curves of the synthesized milled powders obtained under two different conditions for FeMn₃₀Cu₅ biodegradable alloys. One sample curve was related to milling for 1 h with a BPR of 5:1, whereas the other sample curve was related to milling for 10 h with a BPR of 10:1. Both curves exhibited significant peak rises towards the exothermic reaction side up to 400 °C, indicating the evaporation of the incorporated PCA of ethanol [42]. Then, an exothermic peak appeared at approximately 500 °C (point A) and started to decrease at 650 °C (first endothermic peak at point B), which represents the recrystallization starting from point A to the recrystallization end at point B. With an increase in temperature beyond 650 °C, the observed peaks started to increase towards the exothermic side considerably, indicating severe grain growth in the powder particles at approximately 925 °C (point C). With a further increase in temperature, the DSC curves started to decrease towards the endothermic side, indicating considerable absorption of

heat. A sharp drop in the endothermic peak occurred at 1472 °C and 1437 °C for the samples milled for 1 h with a BPR of 5:1 and for the sample milled for 10 h with a BPR of 10:1. This endothermic peak indicated the melting point of the sample. These results clearly demonstrate the significant effect of milling parameters on the thermal behavior. A longer milling time (10 h) with a high BPR value (10:1) resulted in the lowest melting point, owing to the presence of more surface energy in the powder materials. In other words, a longer milling time and high value of BPR introduce more milling energy to the charged materials because of the high velocity of the ball (less mass of powders and more mass of balls in 10:1). The melting point of FeMn₃₀Cu₅ milled for 10 h and a BPR of 10:1 shifted to a lower value, owing to the import of more kinetic energy on the charged materials. The changes in the melting point with milling time and BPR confirmed that the lattice distortion occurred in the sample. Less chemical energy may be necessary to break the chemical bonds during sintering, and, hence, 10 h with the BPR 10:1 sample produces a lower melting temperature [43].

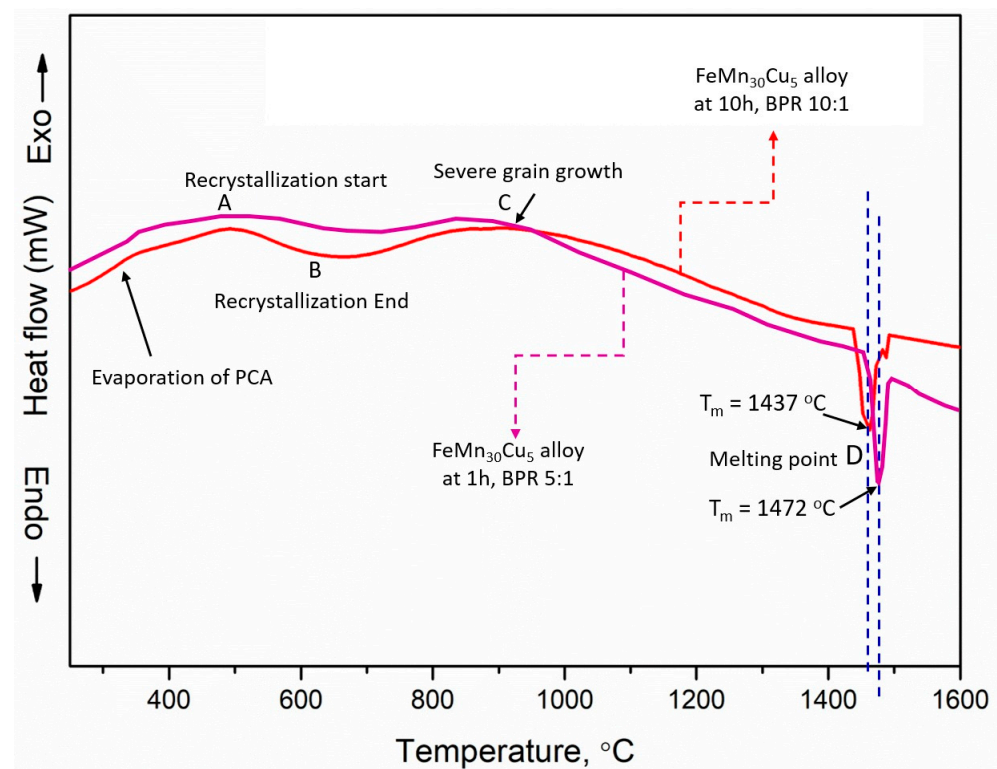


Figure 2. DSC curves of FeMn₃₀Cu₅ for two different milling condition (milling times: 1 and 10 h; BPRs: 5:1 and 10:1).

The X-ray peak profiles of FeMn₃₀Cu₅ biodegradable hot-forged alloys processed with different BPRs (5:1, 10:1, and 15:1) after 10 h of MA are shown in Figure 3. The XRD results showed that the FeMn₃₀Cu₅ biodegradable hot-forged alloy exhibited ferrite iron (α -Fe, BCC, Ref No:01-087-0721), retained austenite iron (γ -Fe, FCC, Ref No:01-088-2324), BCC α -Mn, and FCC α -Cu phases. The formation of ferrite and austenite iron phases in FeMnCu alloys has been reported previously [44–46]. The formation of α -Mn phase is expected to increase the degradation rate, and the incorporation of Cu (more than 3 wt.%) enhances the austenite formation in FeMn alloys, as reported elsewhere [47]. The formation of the austenitic iron phase in the developed alloy is beneficial for MRI in medical applications [44]. Based on the XRD peaks, there were no pure Mn and Cu peaks. The formed α -Mn and α -Cu overlapped with the γ -Fe lattice because of the diffusion of Mn and Cu atoms during sintering and hot-forging. Therefore, the incorporation of the 30 wt.% of Mn and 5 wt.% Cu stabilize the austenite phase, which is expected to enhance the mechanical properties.

Table 2 presents the numeric value of the full width half maximum, peak intensity, center of peak, and area of peak after 10 h with different BPR samples after hot-forging. The observed peak widths and intensities varied as a function of the BPRs. The BPR 5:1 sample exhibited a sharp peak and a high peak intensity (184.51 cps) with a lower peak width (0.3845°), owing to less energy being imported into charged materials, leading to a lower amount of specific energy. However, the BPR 15:1 sample produced a low peak intensity (153.01 cps) and a greater peak width (0.4473°), owing to the greater amount of kinetic/mechanical energy collisions occurring in the charged materials, leading to a higher amount of specific energy. Therefore, a BPR of 15:1 introduces more structural changes for the same milling time of 10 h compared to a BPR of 5:1. This means that more severe plastic deformation, fracturing, and strain hardening are expected to occur in powder materials with a high BPR value of 15:1. These results clearly demonstrate the significant variation in structural changes with milling time and BPR during MA. The presence of a large peak width in the BPR of the 15:1 sample was expected to produce better mechanical properties.

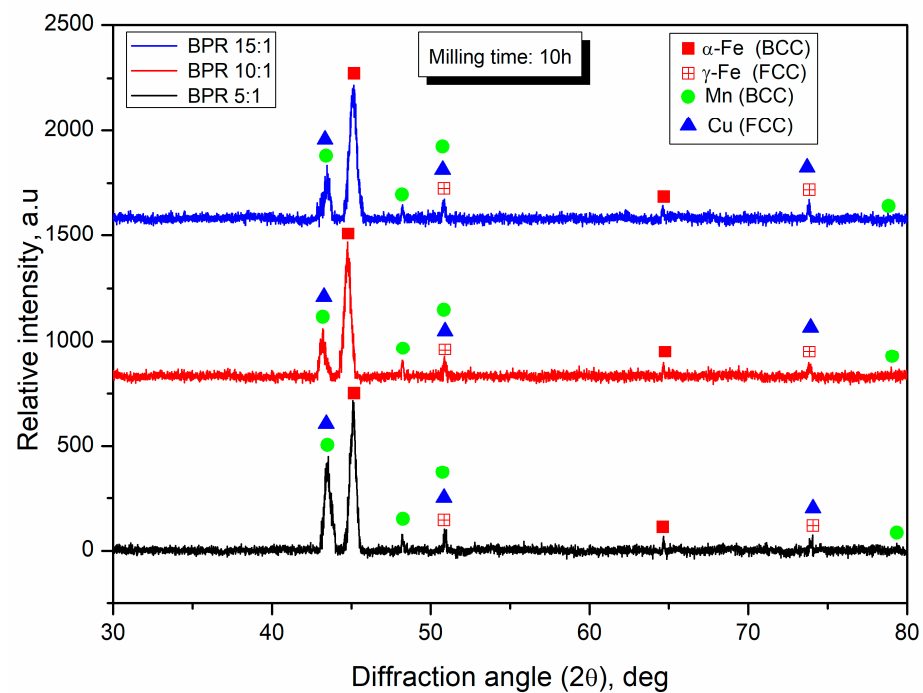


Figure 3. X-ray diffraction peak profiles of FeMn₃₀Cu₅ biodegradable alloys hot-forged and milled at different BPRs (black color: BPR 5:1; red color: BPR 10:1; blue color: BPR 15:1).

Table 2. Influence of BPR on full width half maximum, peak intensity, center of peak, and area of peak after 10 h MA with different BPRs of FeMn₃₀Cu₅ biodegradable hot-forged alloys.

Milling Time, h	Ball-to-Powder Ratio	BCC-Mn Peak				BCC-Fe Peak			
		Center of Peak, Deg	Full Width Half Maximum, Deg	Peak Intensity, Cps	Area of Peak	Center of Peak, Deg	Full Width Half Maximum, Deg	Peak Intensity, Cps	Area of Peak
10	5:1	43.51	0.3845	184.51	76.76	45.10	0.3868	635.15	296.74
10	10:1	43.44	0.4307	167.41	80.69	44.92	0.4251	588.72	307.91
10	15:1	43.20	0.4473	153.01	85.78	44.76	0.4601	556.81	343.17

3.2. FE-SEM Microstructural Analyses of Hot-Forged Alloys

Figure 4 shows the FE-SEM microstructures of chemically etched FeMn₃₀Cu₅ hot-forged biodegradable alloys processed under different milling conditions. The results

clearly demonstrate the significant differences in the microstructures obtained under the corresponding milling conditions. The hot-forged alloy milled for 1 h with a BPR of 5:1 exhibited a coarse ferrite-iron phase (α -Fe) with an average grain size of $72 \pm 4.5 \mu\text{m}$ (Figure 4a). Hot-forged alloys milled at 1 h with BPR 10:1 and BPR 15:1 samples produced the average ferrite grain size of $50 \pm 3.6 \mu\text{m}$ (Figure 4b) and $38.6 \pm 4.7 \mu\text{m}$ (Figure 4c), respectively. The observed α -Fe grains started to decrease considerably with a BPR of 10:1 and slightly with a BPR of 15:1 compared with a BPR of 5:1 for the same milling time of 1 h due to more grain refinement with increasing BPR. However, with increasing BPR for the same milling time of 1 h, the observed porosity also increased, indicating the introduction of more surface energy and dislocations lead to increased porosity [37,48]. Furthermore, at a shorter milling time of 1 h, the FCC-Cu coarse phase (white region in Figure 4a–c) was observed in the hot-forged alloys, indicating the non-dissolution of Cu atoms in the α -Fe lattice, owing to the low milling energy introduced in the charged materials.

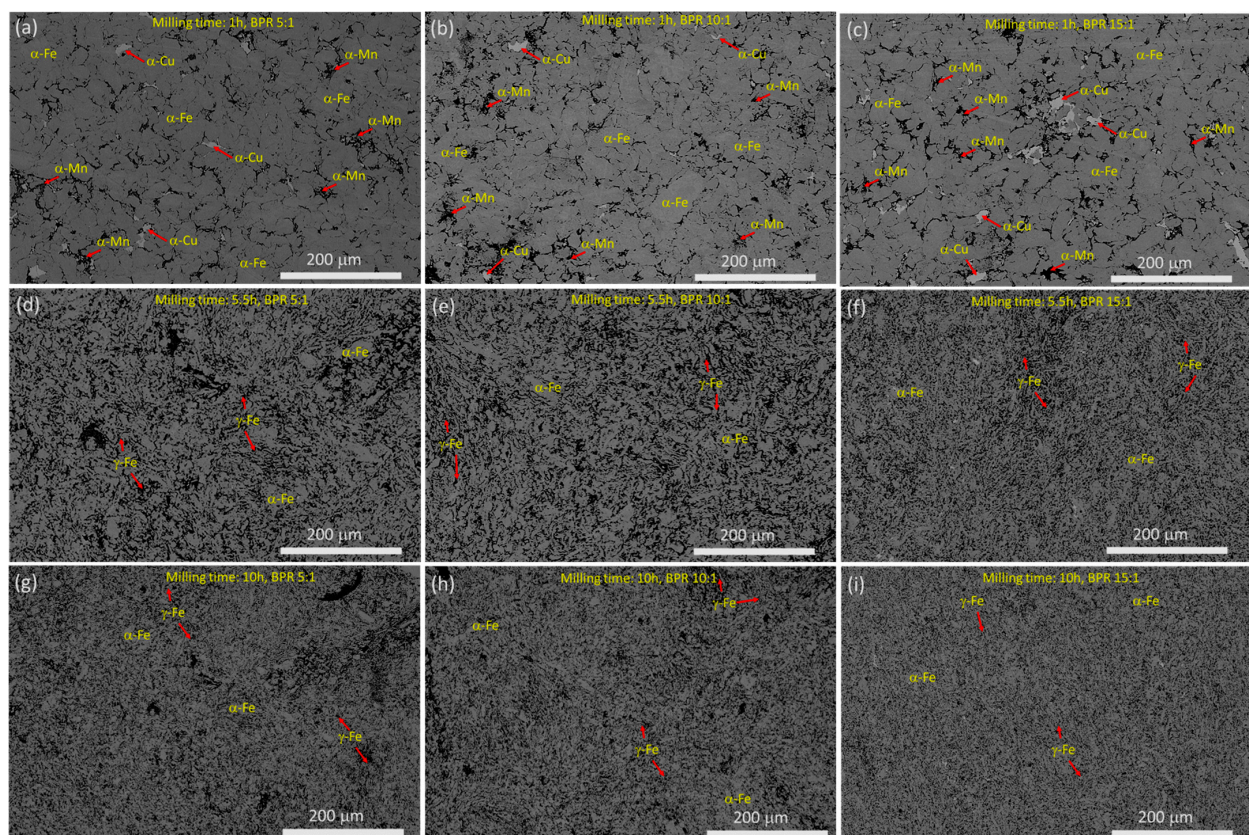


Figure 4. FE-SEM microstructures of $\text{FeMn}_{30}\text{Cu}_5$ hot-forged biodegradable alloys processed at different milling conditions: (a) 1 h with BPR 5:1; (b) 1 h with BPR 10:1; (c) 1 h with BPR 15:1; (d) 5.5 h with BPR 5:1; (e) 5.5 h with BPR 10:1; (f) 5.5 h with BPR 15:1; (g) 10 h with BPR 5:1; (h) 10 h with BPR 10:1; (i) 10 h with BPR 15:1.

With increasing milling time from 1 h to 5.5 h, hot-forged alloys produced an average α -Fe grain size of $16.8 \pm 2.7 \mu\text{m}$, $9.5 \pm 2.4 \mu\text{m}$, and $5.5 \pm 1.8 \mu\text{m}$ for BPR 5:1, BPR 10:1, and BPR 15:1, respectively (Figure 4d–f). These results explain the considerable reduction in grain size with increasing milling times and BPRs leading to considerable absorption of heat. After milling for 5.5 h, the hot-forged alloys exhibited a retained austenite-iron (γ -Fe) phase in addition to the α -Fe phase, owing to severe plastic deformation and dislocations that occurred in the structure, which promoted the formation of the γ -Fe phase after sintering and hot-forging [37,48]. The formation of the γ -Fe phase was expected to enhance its mechanical properties. In addition, the coarse FCC-Cu phase was not observed in the SEM microstructures (no white region, Figure 4d–f), indicating a solid solution of FCC-Cu

atoms in the Fe lattice. With further increasing of milling time up to 10 h, hot-forged alloys exhibited the average grain size of $1.1 \pm 0.8 \mu\text{m}$, $0.64 \pm 0.4 \mu\text{m}$, and $0.38 \pm 0.3 \mu\text{m}$ for BPR 5:1, BPR 10:1, and BPR 15:1, respectively (Figure 4g–i). The results clearly demonstrate that drastic structural changes occurred with increasing milling time and BPR, which led to different microstructural evolutions. To show the formation of $\gamma\text{-Fe}$, $\alpha\text{-Fe}$, $\alpha\text{-Mn}$, and $\alpha\text{-Cu}$ phases, FE-SEM with higher magnification was carried out, and the results are shown in Figure 5. The $\text{FeMn}_{30}\text{Cu}_5$ hot-forged alloy for 1 h with the BPR 5:1 sample exhibited $\gamma\text{-Fe}$, $\alpha\text{-Fe}$, $\alpha\text{-Mn}$, and $\alpha\text{-Cu}$ phases [44,47], in which a non-uniform distribution of the rich $\alpha\text{-Mn}$ phase was observed. The non-uniform distribution of the $\alpha\text{-Mn}$ -rich phase was attributed to the low-energy import in the charged materials. However, with increasing milling time for the same BPR (5:1), the sintered and hot-forged $\text{FeMn}_{30}\text{Cu}_5$ biodegradable alloys exhibited a uniform distribution and solid solutions of $\alpha\text{-Mn}$ and $\alpha\text{-Cu}$ phases in addition to $\gamma\text{-Fe}$ and $\alpha\text{-Fe}$ phases. These results clearly indicate that severe structural refinement occurs with increasing milling time. In other words, the charged materials are usually subjected to more severe plastic deformation with increasing milling time and BPR, leading to refined internal structures (reduction in grains, changes in lattice strain, and changes in dislocations, etc. [37,48]) and increases in stored energy, which also promote the austenite-iron phase after sintering and hot-forging. The stored energy with increasing milling time and BPR promotes phase transformation, owing to a decrease in activation energy [49]. The formation of the austenite-iron phase with increasing milling time was observed and reported by several researchers [50].

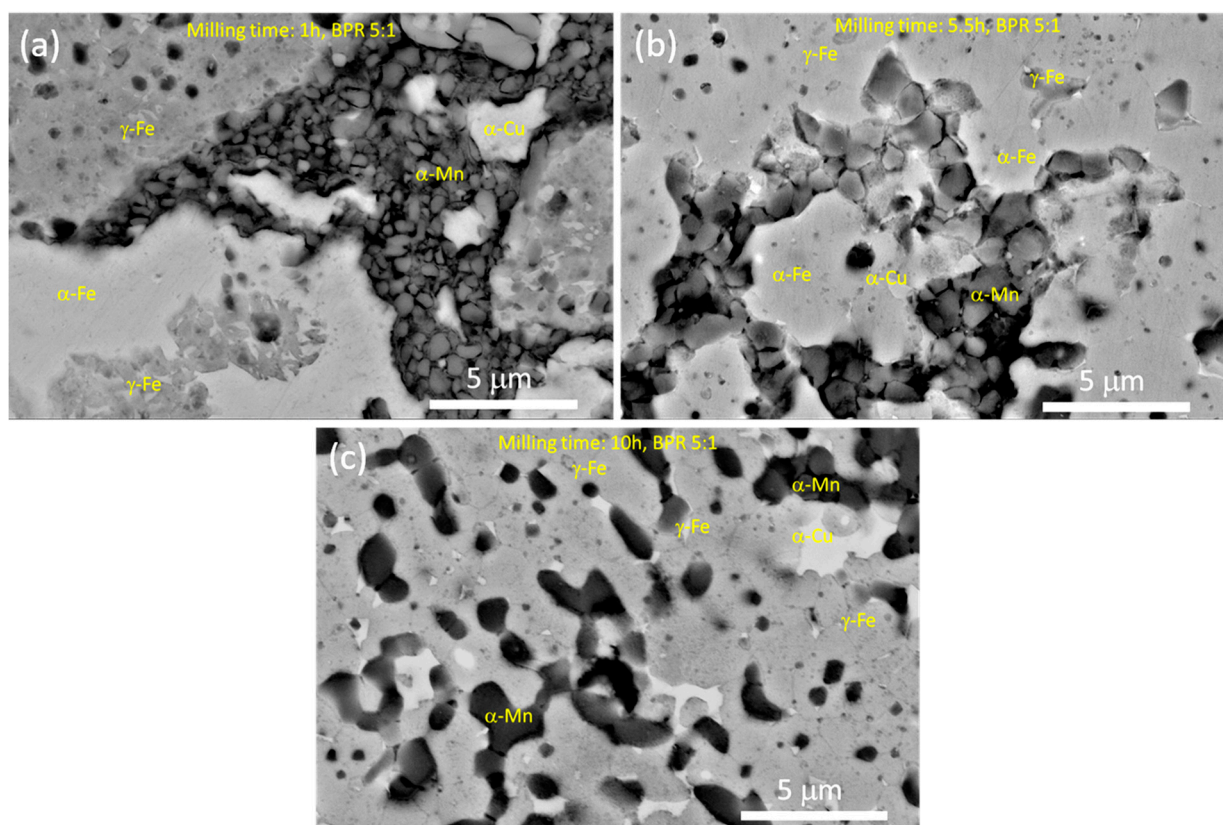


Figure 5. Various phase observations at higher magnification of E-SEM microstructures of $\text{FeMn}_{30}\text{Cu}_5$ hot-forged biodegradable alloys processed at different milling conditions: (a) 1 h with BPR 5:1; (b) 5.5 h with BPR 5:1; (c) 10 h with BPR 5:1.

To show the alloy formation and dispersion of incorporated elements in the $\text{FeMn}_{30}\text{Cu}_5$ alloys under different milling conditions, FE-SEM with live and elemental maps was carried out on hot-forged alloys, and the same is shown in Figure 6a–c for 5.5 h with BPR 5:1, 5.5 h

with BPR 10:1, and 10 h with BPR 15:1 samples, respectively. The results demonstrated that the incorporated elements were uniformly dispersed, indicating the successful formation of the alloy. In addition, coarse FCC-Cu spots were observed in 5.5 h with the BPR 5:1 sample because of the low energy imported into the alloy (Figure 6a), whereas uniform and ultra-fine dispersion of FCC-Cu atoms was observed in 10 h with the BPR 15:1 sample (Figure 6c) because of the high-energy import in the alloy, leading to the introduction of more dislocations [37]; consequently, this sample may be expected to produce improved mechanical performance.

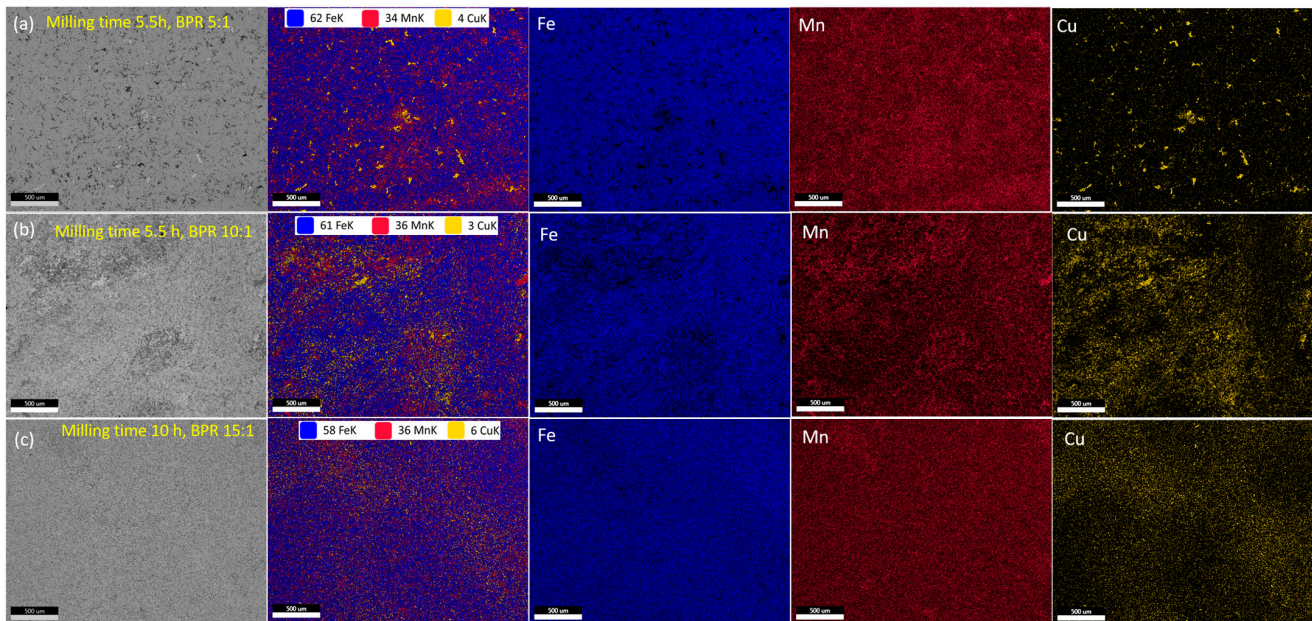


Figure 6. FE-SEM live and elemental mapping of FeMn₃₀Cu₅ hot-forged biodegradable alloys processed at different milling conditions: (a) 5.5 h with BPR 5:1; (b) 5.5 h with BPR 10:1; (c) 10 h with BPR 15:1. First column represents the HR-SEM microstructures; second column represents the elemental overlay map; third, fourth, and fifth columns represent the elemental map of Fe, Mn, and Cu, respectively.

The FE-SEM with EBSD analyses, in terms of the colored grain map and phase contrast map of the hot-forged FeMn₃₀Cu₅ alloys, are shown in Figure 7 under different milling conditions. The EBSD colored grain map of hot-forged FeMn₃₀Cu₅ alloys processed for 10 h with BPR 5:1 (Figure 7a) exhibited fine grains of both austenite-Fe and ferrite-Fe phases. The average grain size based on EBSD colored grain map was $0.92 \pm 0.53 \mu\text{m}$, which is matched with the size obtained from FE-SEM etched microstructures (Figure 4g). The corresponding phase contrast map is shown in Figure 6b, in which 72.34% of retained austenite (FCC) and 27.66% of ferrite (BCC) phases were obtained in 10 h with BPR 5:1 hot-forged alloy. The EBSD colored map of hot-forged FeMn₃₀Cu₅ alloys processed for 10 h with BPR 10:1 (Figure 7c) produced ultrafine grains of both austenite and ferrite phases [37,44]. The average grain size obtained from EBSD colored map was $0.54 \pm 0.25 \mu\text{m}$, which is also matched with the results obtained from FE-SEM microstructure of the same sample (Figure 4h). Figure 7d shows the corresponding phase contrast map of Figure 7c, in which 84.20% of retained austenite (FCC) and 15.8% of ferrite (BCC) phases were obtained in 10 h with BPR 10:1 sample. These results indicate that increasing the BPRs promoted the formation of the retained austenite phase (FCC) and refined the grain size [44]. This is attributed to additional structural refinements, dislocations, and increases in the specific surface energy produced by high energy mechanical collisions [37,44,48]. The grain size distribution with area fraction and the distribution of the misorientation angle with number fraction were examined to show the structural changes and grain refinement, as shown in

Figure 8. Based on Figure 8a,c, it is clear that the distributions of grain size were shifted towards the left in 10 h with the BPR 10:1 sample compared to 10 h with the BPR 5:1 sample, indicating structural changes and grain refinement with increasing BPR (Table 2). Similarly, distribution of misorientation angle at 10 h with BPR10:1 sample exhibited more percentage of high-angle grain boundaries, HAGBs (57.70%), and shifted to higher angle compared to 10 h with BPR 5:1 sample, which produced HAGBs of 50.56%. These results demonstrate that more grain refinement and structural changes occurred at high BPR values (Table 2 and Figure 4).

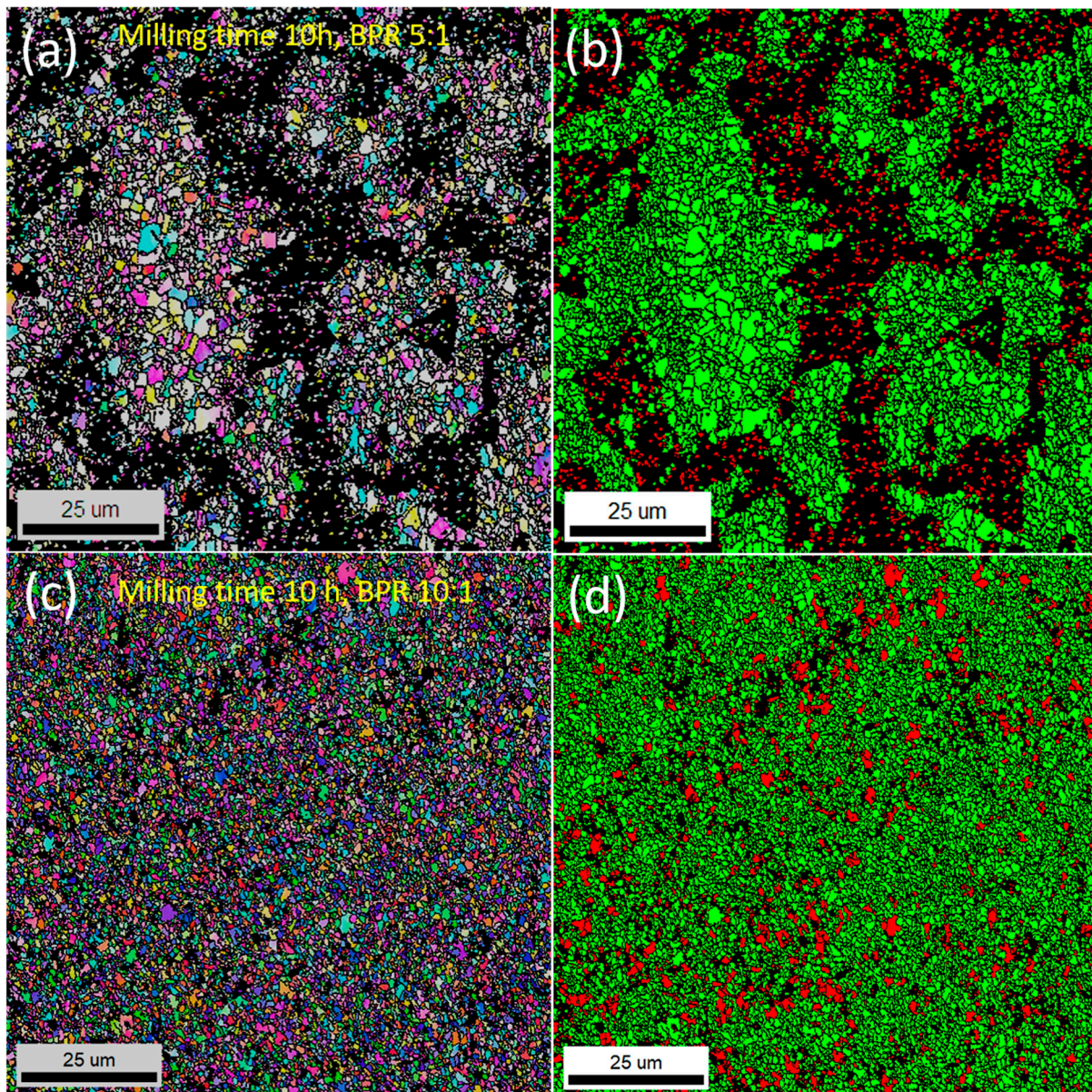


Figure 7. EBSD analyses on FeMn₃₀Cu₅ hot-forged biodegradable alloys processed at different milling conditions: (a) colored map of 10 h and BPR 5:1 sample; (b) phase contrast map corresponding to (a); (c) colored map of 10 h and BPR 10:1 sample; (d) phase contrast map corresponding to (c); Here in phase contrast map of (b,d), green represent FCC-austenite, and red represent BCC-ferrite phases.

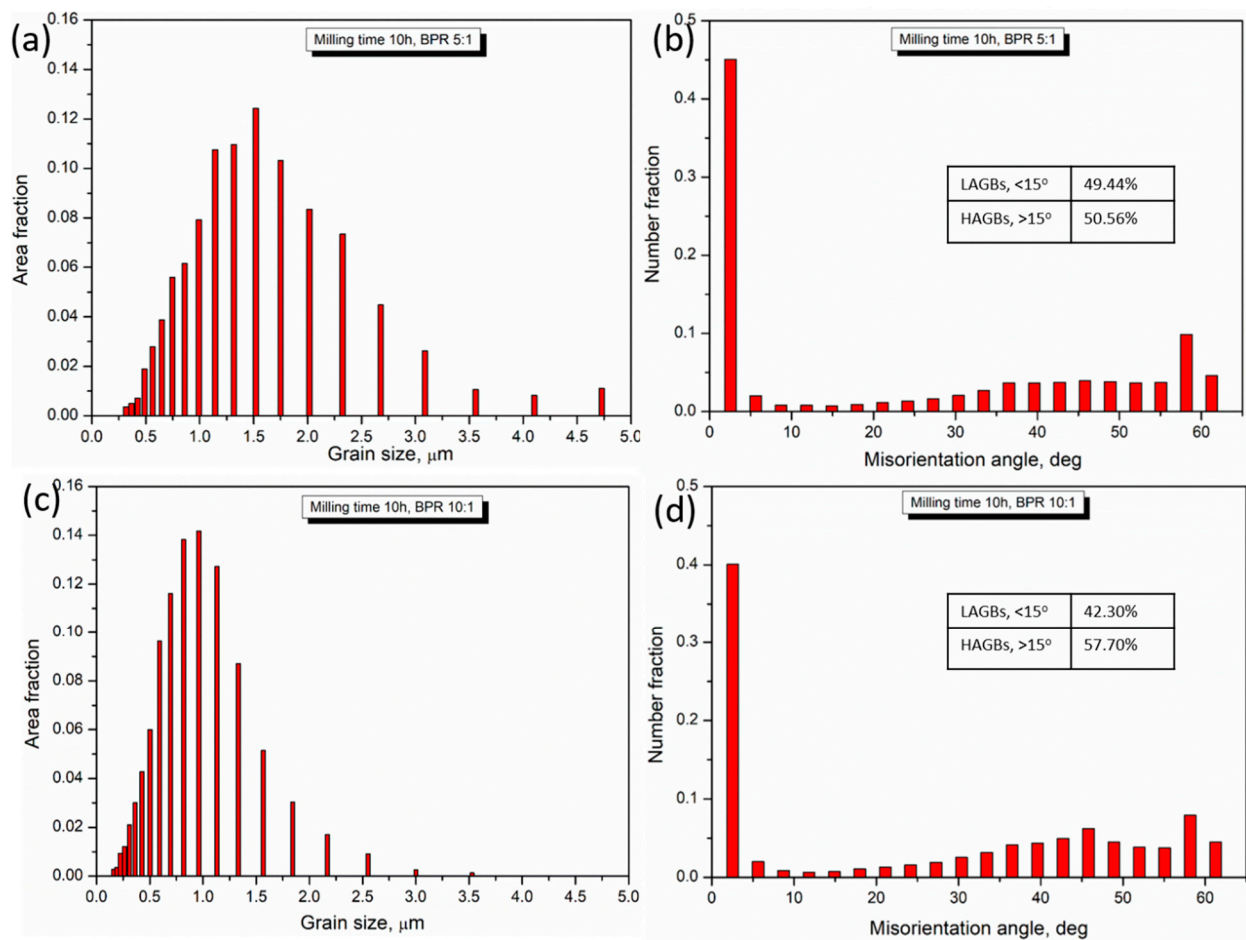


Figure 8. Grain size distribution Vs area fraction of FeMn₃₀Cu₅ hot-forged biodegradable alloys processed at different milling conditions: (a) 10 h and BPR 5:1 sample; (c) 10 h and BPR 10:1; Misorientation angle Vs number fraction of FeMn₃₀Cu₅ hot-forged biodegradable alloys processed at different milling conditions: (b) 10 h and BPR 5:1 sample; (d) 10 h and BPR 10:1.

3.3. Examination of Percentage Theoretical Density and Vickers Hardness Strength

Figure 9 shows the variation in the percentage theoretical density of the FeMn₃₀Cu₅ hot-forged biodegradable alloys with the milling time (1, 5.5, and 10 h), and BPRs (5:1, 10:1, and 15:1). The measured percentage theoretical densities and error bars are listed in Table 3. The measured percentage theoretical density started to decrease considerably with the milling time and BPRs. Both the parameters were significantly affected. For instance, at 10 h, the measured percentage theoretical density values were 84.45, 83.78, and 82.14% for BPRs of 5:1, 10:1, and 15:1, respectively. The decreased percentage theoretical densities of BPR 10:1 and BPR 15:1 samples compared to the BPR 5:1 sample were 0.80% and 2.73%, respectively. Similarly, at BPR 10:1, the measured percentage theoretical density values were 86.78, 84.36, and 83.78% for 1, 5.5, and 10 h respectively. The decreased percentage theoretical density of 5.5 h and 10 h samples compared to 1 h sample was 2.79% and 3.46%, respectively. These results clearly indicate that with increasing milling times and BPRs, structural refinements, severe plastic deformation, and dislocations increased significantly in the structure leading to increased structural defects (Table 2 and Figure 4) [38,44]. Hence, the measured theoretical density began to decrease with increasing milling time and BPRs.

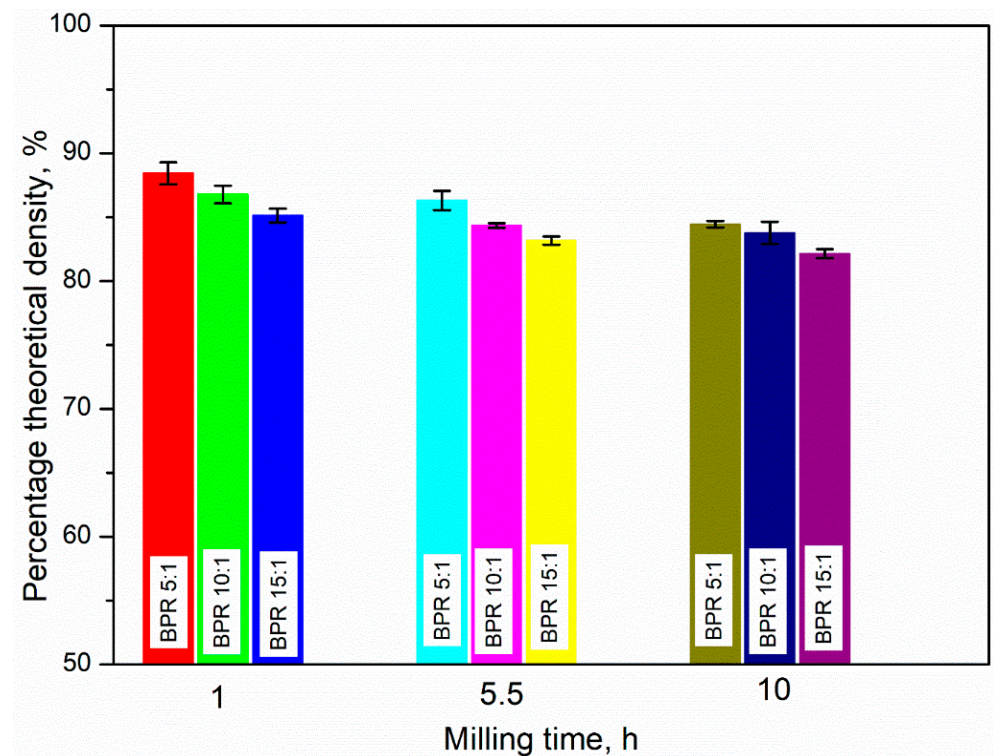


Figure 9. Variation in percentage theoretical density with the milling time and BPRs for FeMn₃₀Cu₅ biodegradable alloys.

Table 3. Variation of milling times and ball-to-powder ratios on percentage theoretical density, Vickers hardness strength, and mechanical properties.

Milling Time, h	Ball-to-Powder Ratio	Percentage Theoretical Density	Vickers Hardness Strength, HV	Mechanical Properties			
				Yield Strength, MPa	Strain at Yield Point	Ultimate Strength, MPa	Strain at Ultimate Point
1	5:1	88.45 ± 0.85	76.23 ± 3.8	497.25 ± 4.8	2.70	1200.45 ± 6.5	33.71
1	10:1	86.78 ± 0.68	80.45 ± 2.5	529.32 ± 3.6	2.50	1304.87 ± 7.5	32.36
1	15:1	85.14 ± 0.55	86.32 ± 1.7	560.52 ± 3.1	2.42	1399.46 ± 5.9	31.88
5.5	5:1	86.32 ± 0.75	87.68 ± 1.4	572.76 ± 2.9	2.68	1380.49 ± 6.4	33.27
5.5	10:1	84.36 ± 0.18	93.34 ± 2.1	638.81 ± 5.2	2.65	1513.64 ± 4.8	32.01
5.5	15:1	83.18 ± 0.31	98.42 ± 1.1	684.15 ± 4.6	2.82	1560.51 ± 5.3	31.43
10	5:1	84.45 ± 0.25	102.35 ± 3.2	640.15 ± 3.4	2.43	1617.93 ± 6.1	32.57
10	10:1	83.78 ± 0.88	108.78 ± 2.3	718.84 ± 2.7	2.55	1714.95 ± 5.5	31.40
10	15:1	82.14 ± 0.35	112.47 ± 2.0	748.38 ± 3.6	2.49	1788.17 ± 4.9	30.58

Figure 10 shows the variation in the Vickers hardness strength of the FeMn₃₀Cu₅ hot-forged biodegradable alloys processed at different milling times (1, 5.5, and 10 h) and BPRs (5:1, 10:1, and 15:1); the values are listed in Table 3. The results demonstrated that the measured Vickers hardness strength increased significantly with the milling time and BPRs, owing to the increase in the severe plastic deformation of charged materials, dislocations, structural refinements, strain hardening, and specific energy (Table 2 and Figure 4) [38]. For instance, at 10 h, the measured Vickers hardness values were 102.35, 108.78, and 112.47 HV for the BPRs of 5:1, 10:1, and 15:1, respectively. The increased percentage of Vickers hardness values of BPR 10:1 and BPR 15:1 samples compared to the BPR 5:1 sample was 6.28% and

9.88%, respectively. Similarly, at BPR 10:1, the Vickers hardness values were 80.45, 93.34, and 108.78% at 1, 5.5, and 10 h respectively. The increased percentages of Vickers hardness values of 5.5 h and 10 h samples compared with the 1 h sample were 16.02% and 35.21%, respectively. These results clearly demonstrate that the measured Vickers hardness strength was influenced more by the milling time than the BPR because of the increase in mechanical kinetic energy collisions owing to the lower amount of powder and high velocity of the balls for the same milling time [44]. In addition, with increasing BPRs, the formation of the retained austenite (FCC) structure started to increase, which might be attributed to the enhancement of the Vickers hardness strength (Figures 4 and 7).

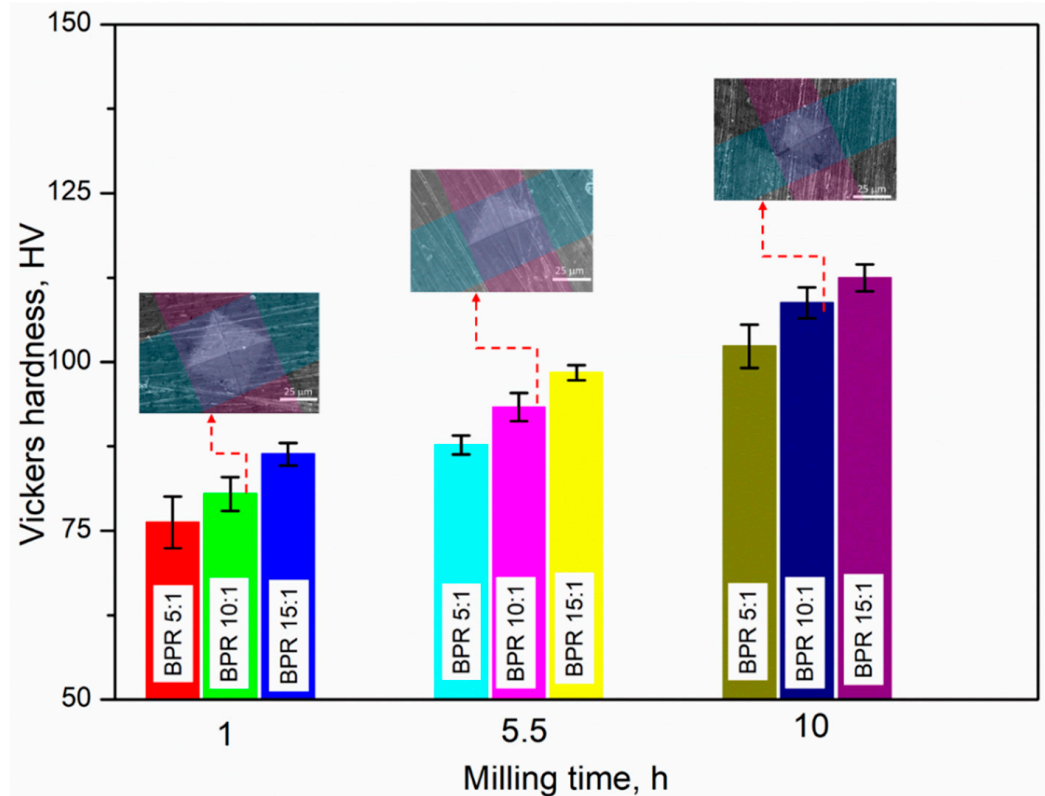


Figure 10. Variation in Vickers hardness strength with the milling time and BPRs for FeMn₃₀Cu₅ biodegradable alloys.

3.4. Examination of Mechanical Behavior by Compressive Stress–Strain Curves

The compressive stress–strain curves of the FeMn₃₀Cu₅ hot-forged biodegradable alloys processed under different milling conditions are shown in Figure 11. The mechanical properties calculated based on Equations (1) and (2) are listed in Table 3. The compressive stress–strain curves showed that the compressive stress–strain curves started to increase significantly with milling time and increased considerably with increasing BPRs. With increasing milling time, the strain hardening and flow softening behavior began to increase in all the BPRs after yielding. The 10 h milled samples exhibited the dominance of strain hardening compared to flow softening because of more structural refinements, entangled dislocations, and the presence of more specific energy produced by longer milling times [37,44]. In addition, the shifting of the compressive stress–strain curves upwards with BPR was attributed to an increase in the austenite phase in the internal structures (Figures 4 and 7). The variations in the compressive yield and ultimate strengths with milling time and BPRs are shown in Figure 12a,b, respectively. From Figure 12, it is clear that both milling times (1, 5.5, and 10 h) and BPRs (5:1, 10:1, and 15:1) significantly influenced the yield and ultimate strengths. For example, at 1 h, the yield strength was 497.25, 529.32, and 560.52 MPa for BPR5:1, BPR10:1, and BPR 15:1, respectively. The increasing percentage of yield strength of BPR 10:1 and BPR 15:1 samples when compared

to the BPR 5:1 sample was 6.50 and 12.71%, respectively, which confirmed the presence of more structural refinements and dislocations [37,44]. Similarly, at a BPR of 10:1, the yield strengths were 529.32, 638.81, and 718.84 at 1, 5.5, and 10 h, respectively. The increasing percentage of yield strength of 5.5 and 10 h samples compared to 1 h sample was 20.68 and 35.80%, respectively. This result indicates that at a BPR of 10:1, the increase in milling time significantly affected the yield strength of the $\text{FeMn}_{30}\text{Cu}_5$ hot-forged alloys owing to more mechanical energy, strain hardening, dislocations imported on the charged materials, grain refinements, and more structural changes (Figures 4, 7 and 8 [48]). The same phenomena were observed for the ultimate strengths of the developed alloys processed under different milling conditions. Overall, by considering strength and more deformation by strain, the 10 h with BPR 15:1 sample exhibited considerable ultimate strength (1788 MPa) and strain (30.58%), which may be recommended for biodegradable applications.

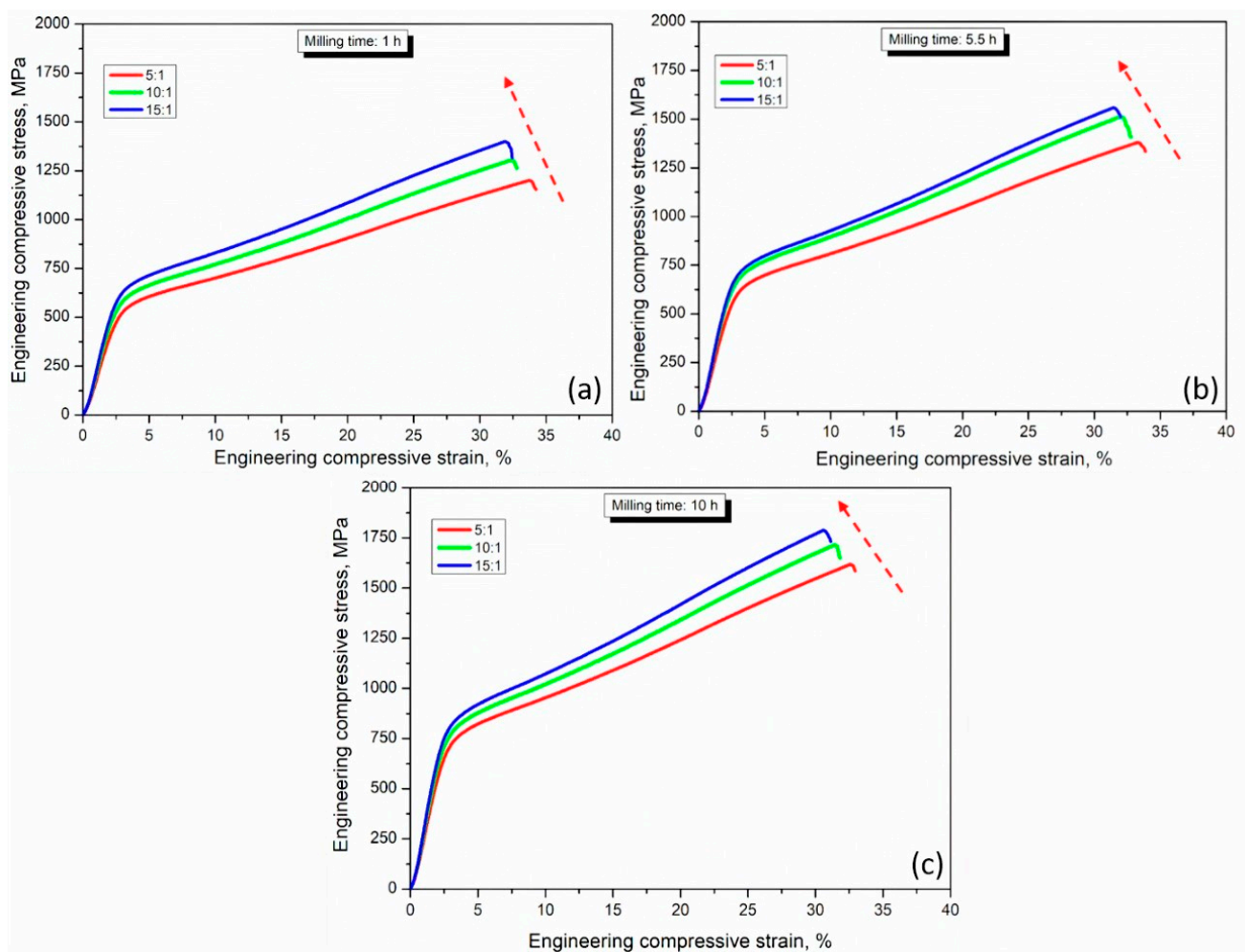


Figure 11. Engineering compressive stress–strain curves of $\text{FeMn}_{30}\text{Cu}_5$ hot-forged biodegradable alloys processed under different milling conditions: (a) 1 h and BPRs (5:1, 10:1, and 15:1); (b) 5.5 h and BPRs (5:1, 10:1, and 15:1); (c) 10 h and BPRs (5:1, 10:1, and 15:1). The arrow indicates the significance of mechanical milling parameters on compressive stress–strain performance upwards.

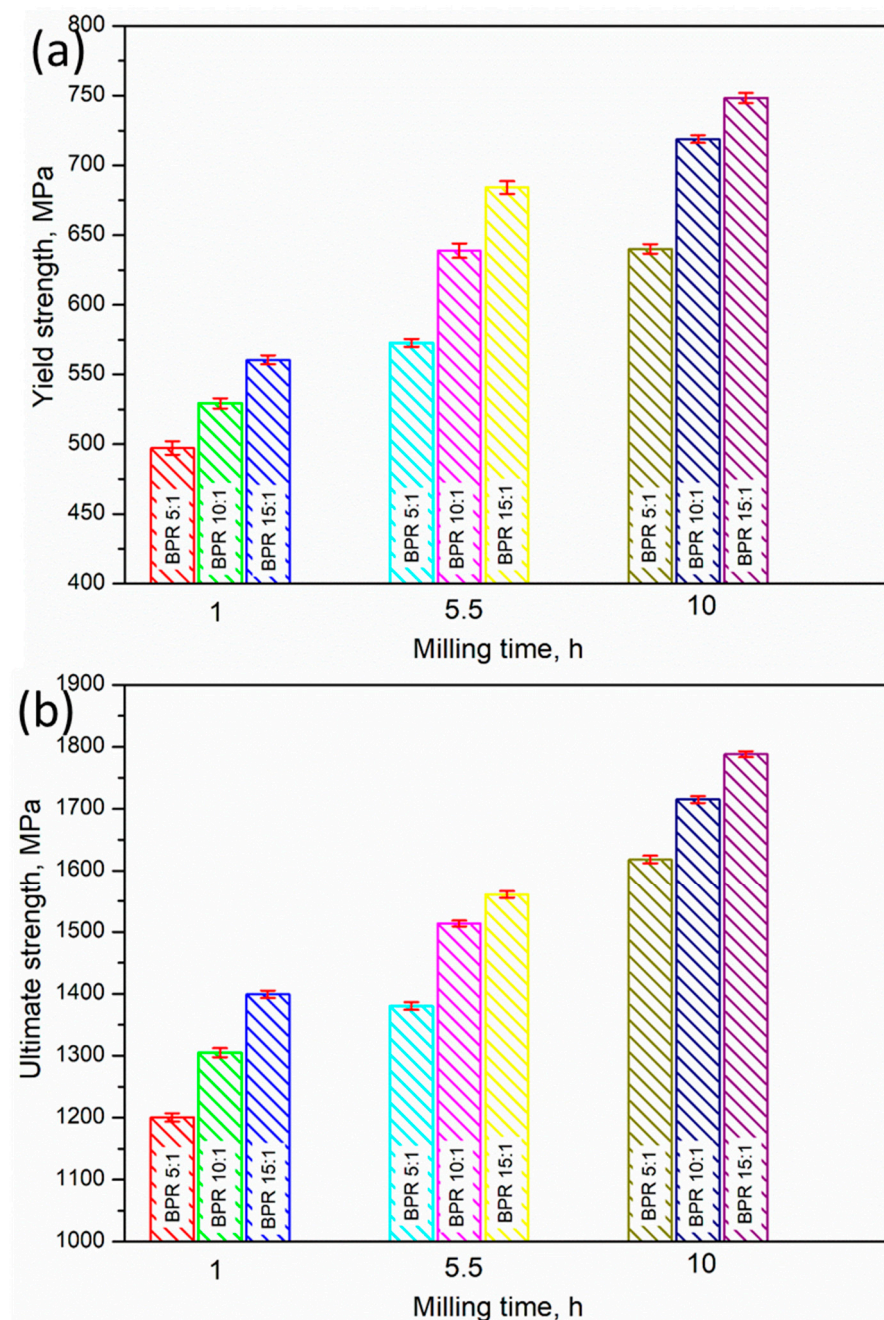


Figure 12. Variation in yield strength and ultimate strength with milling time and BPRs for FeMn₃₀Cu₅ biodegradable alloys: (a) yield strength; (b) ultimate strength.

4. Conclusions

In this study, FeMn₃₀Cu₅ hot-forged biodegradable alloys were developed under different milling conditions in which the milling times and BPRs were varied. Powders were synthesized by MA, followed by hot-compaction, sintering in a medium-frequency furnace, and hot-forging. The microstructural evolution and mechanical behavior were examined in detail. From this study, the following conclusions were drawn.

- Based on the DSC results of the synthesized powders, the observed melting point of the FeMn₃₀Cu₅ biodegradable alloy powders milled for 10 h and a BPR of 10:1 was shifted to a lower value (1437 °C), owing to the import of more kinetic energy by mechanical collisions and the presence of more specific energy.

- The X-ray peak profile results demonstrated the formation of ferrite (α -Fe, BCC), retained austenite (γ -Fe, FCC), FCC-Mn, and FCC-Cu phases in the hot-forged samples. The BPR 15:1 sample exhibited a reduction in the peak intensity and an increase in peak width, owing to more kinetic/mechanical energy collisions occurring in the charged materials, leading to a greater amount of specific energy and grain refinement.
- The FE-SEM microstructures showed that after milling for 5.5 h, the hot-forged alloys exhibited a retained austenite-iron (γ -Fe) phase in addition to the α -Fe phase, owing to severe plastic deformation and dislocations occurring in the structure, leading to the promotion of the γ -Fe phase after sintering and hot-forging.
- The FE-SEM live and elemental map results confirm that the incorporated elements were dispersed uniformly after 5.5 h of MA, indicating the successful formation of an alloy when milling for 5.5 h with any BPRs (5:1, 10:1, or 15:1).
- The measured percentage theoretical density results showed that the percentage theoretical density started to decrease significantly with the milling time and BPRs. Furthermore, the Vickers hardness strength increased significantly with milling time and BPRs, owing to the increase in the severe plastic deformation of the charged materials, dislocations, structural refinements, strain hardening, and specific energy.
- The mechanical behavior in terms of compressive stress–strain curves showed that the stress–strain curves started to increase significantly with the milling time and increased considerably with the BPRs. With increasing milling time, the strain hardening and flow softening behavior began to increase in all the BPRs after yielding. In addition, both milling times (1, 5.5, and 10 h), and BPRs (5:1, 10:1, and 15:1) significantly influenced the yield and ultimate strengths, owing to the structural changes and grain refinement by MA.
- Overall, by considering strength and more deformation by strain, the 10 h with BPR 15:1 sample exhibited considerable ultimate strength (1788 MPa) and strain (30.58%), which may be recommended for biodegradable/biomedical applications.

Author Contributions: Conceptualization, S.S. and H.R.A.; methodology, S.S., H.R.A. and A.S.A.; formal analysis, S.S., H.R.A., S.A.E. and A.-b.H.M.; investigation, S.S., H.R.A., A.S.A. and B.A.; data curation, S.S. and H.R.A., B.A., S.A.E. and A.-b.H.M.; writing—original draft preparation, S.S.; writing—review and editing, S.S., H.R.A., B.A. and A.S.A. All authors have read and agreed to the published version of the manuscript.

Funding: This research was funded by Qassim University, represented by the Deanship of Scientific Research, under the number (5583-qec-2019-2-2-1).

Data Availability Statement: The experimental datasets obtained from this research work and then the analyzed results during the current study are available from the corresponding author on reasonable request.

Acknowledgments: The authors gratefully acknowledge Qassim University, represented by the Deanship of Scientific Research, on the financial support for this research under the number (5583-qec-2019-2-2-1) during the academic year 1440 AH/2019 AD.

Conflicts of Interest: The authors declare no conflict of interest.

References

1. Gašior, G.; Szczepański, J.; Radtke, A. Biodegradable iron-based materials—What was done and what more can be done? *Materials* **2021**, *14*, 3381. [[CrossRef](#)]
2. Francis, A.; Yang, Y.; Virtanen, S.; Boccaccini, A.R. Iron and iron-based alloys for temporary cardiovascular applications. *J. Mater. Sci. Mater. Med.* **2015**, *26*, 1–16. [[CrossRef](#)]
3. Gorejová, R.; Haverová, L.; Oriňaková, R.; Oriňak, A.; Oriňak, M. Recent advancements in Fe-based biodegradable materials for bone repair. *J. Mater. Sci.* **2019**, *54*, 1913–1947. [[CrossRef](#)]
4. Oriňaková, R.; Oriňak, A.; Giretová, M.; Medvecký, L.; Kupková, M.; Hrubovčáková, M.; Maskal'ová, I.; Macko, J.; Kal'avský, F. A study of cytocompatibility and degradation of iron-based biodegradable materials. *J. Biomater. Appl.* **2016**, *30*, 1060–1070. [[CrossRef](#)] [[PubMed](#)]

5. de Andrade, L.M.; Paternoster, C.; Chevallier, P.; Gambaro, S.; Mengucci, P.; Mantovani, D. Surface processing for iron-based degradable alloys: A preliminary study on the importance of acid pickling. *Bioact. Mater.* **2022**, *11*, 166–180. [[CrossRef](#)]
6. Huang, C.-C.; Lam, T.-N.; Amalia, L.; Chen, K.-H.; Yang, K.-Y.; Muslih, M.R.; Singh, S.S.; Tsai, P.-I.; Lee, Y.-T.; Jain, J. Tailoring grain sizes of the biodegradable iron-based alloys by pre-additive manufacturing microalloying. *Sci. Rep.* **2021**, *11*, 1–12. [[CrossRef](#)]
7. Dargusch, M.S.; Dehghan-Manshadi, A.; Shahbazi, M.; Venezuela, J.; Tran, X.; Song, J.; Liu, N.; Xu, C.; Ye, Q.; Wen, C. Exploring the Role of Manganese on the Microstructure, Mechanical Properties, Biodegradability, and Biocompatibility of Porous Iron-Based Scaffolds. *ACS Biomater. Sci. Eng.* **2019**, *5*, 1686–1702. [[CrossRef](#)]
8. Kumar, K.; Das, A.; Prasad, S.B. Biodegradable metal matrix composites for orthopedic implant applications: A review. *Adv. Eng. Mater.* **2021**, 557–565. [[CrossRef](#)]
9. Jain, T.; Jain, J.K.; Saxena, K.K. Design and Comprehensive Study of Biodegradable Zinc-based Implants for Bio-medical Applications. *Adv. Mater. Process. Technol.* **2021**, 1–18. [[CrossRef](#)]
10. Waizy, H.; Seitz, J.-M.; Reifenrath, J.; Weizbauer, A.; Bach, F.-W.; Meyer-Lindenberg, A.; Denkena, B.; Windhagen, H. Biodegradable magnesium implants for orthopedic applications. *J. Mater. Sci.* **2013**, *48*, 39–50. [[CrossRef](#)]
11. Kubásek, J.; Vojtěch, D.; Jablonská, E.; Pospíšilová, I.; Lipov, J.; Ruml, T. Structure, mechanical characteristics and in vitro degradation, cytotoxicity, genotoxicity and mutagenicity of novel biodegradable Zn–Mg alloys. *Mater. Sci. Eng. C* **2016**, *58*, 24–35. [[CrossRef](#)] [[PubMed](#)]
12. Ding, Y.; Lin, J.; Wen, C.; Zhang, D.; Li, Y. Mechanical properties, corrosion, and biocompatibility of Mg-Zr-Sr-Dy alloys for biodegradable implant applications. *J. Biomed. Mater. Res. Part B Appl. Biomater.* **2018**, *106*, 2425–2434. [[CrossRef](#)] [[PubMed](#)]
13. Bairagi, D.; Mandal, S. A comprehensive review on biocompatible Mg-based alloys as temporary orthopaedic implants: Current status, challenges, and future prospects. *J. Magnes. Alloy* **2021**, *10*, 627–669. [[CrossRef](#)]
14. Yuan, W.; Xia, D.; Wu, S.; Zheng, Y.; Guan, Z.; Rau, J.V. A review on current research status of the surface modification of Zn-based biodegradable metals. *Bioact. Mater.* **2022**, *7*, 192–216. [[CrossRef](#)]
15. Li, H.F.; Shi, Z.Z.; Wang, L.N. Opportunities and challenges of biodegradable Zn-based alloys. *J. Mater. Sci. Technol.* **2020**, *46*, 136–138. [[CrossRef](#)]
16. Niu, J.; Tang, Z.; Huang, H.; Pei, J.; Zhang, H.; Yuan, G.; Ding, W. Research on a Zn-Cu alloy as a biodegradable material for potential vascular stents application. *Mater. Sci. Eng. C* **2016**, *69*, 407–413. [[CrossRef](#)] [[PubMed](#)]
17. Schinhammer, M.; Hänzli, A.C.; Löffler, J.F.; Uggowitzer, P.J. Design strategy for biodegradable Fe-based alloys for medical applications. *Acta Biomater.* **2010**, *6*, 1705–1713. [[CrossRef](#)] [[PubMed](#)]
18. Paul, B.; Lode, A.; Placht, A.-M.; Voß, A.; Pilz, S.; Wolff, U.; Oswald, S.; Gebert, A.; Gelinsky, M.; Hufenbach, J. Cell-Material Interactions in Direct Contact Culture of Endothelial Cells on Biodegradable Iron-Based Stents Fabricated by Laser Powder Bed Fusion and Impact of Ion Release. *ACS Appl. Mater. Interfaces* **2021**, *14*, 439–451. [[CrossRef](#)] [[PubMed](#)]
19. Wegener, B.; Sievers, B.; Utzschneider, S.; Müller, P.; Jansson, V.; Rößler, S.; Nies, B.; Stephani, G.; Kieback, B.; Quadbeck, P. Microstructure, cytotoxicity and corrosion of powder-metallurgical iron alloys for biodegradable bone replacement materials. *Mater. Sci. Eng. B* **2011**, *176*, 1789–1796. [[CrossRef](#)]
20. Grodzicka, M.; Gašior, G.; Wiśniewski, M.; Bartmański, M.; Radtke, A. A Simple Replica Method as the Way to Obtain a Morphologically and Mechanically Bone-like Iron-Based Biodegradable Material. *Materials* **2022**, *15*, 4552. [[CrossRef](#)] [[PubMed](#)]
21. Zivic, F.; Grujovic, N.; Pellicer, E.; Sort, J.; Mitrovic, S.; Adamovic, D.; Vulovic, M. Biodegradable metals as biomaterials for clinical practice: Iron-based materials. In *Biomaterials in Clinical Practice*; Springer: Cham, Switzerland, 2018; pp. 225–280.
22. Buchanan, F.J. *Degradation Rate of Bioresorbable Materials: Prediction and Evaluation*, 1st ed.; Woodhead Publishing: Cambridge, UK, 2008.
23. Phinikarides, A.; Kindyni, N.; Makrides, G.; Georghiou, G.E. Review of photovoltaic degradation rate methodologies. *Renew. Sustain. Energy Rev.* **2014**, *40*, 143–152. [[CrossRef](#)]
24. Rafiee, K.; Feng, Q.; Coit, D.W. Reliability modeling for dependent competing failure processes with changing degradation rate. *IIE Trans.* **2014**, *46*, 483–496. [[CrossRef](#)]
25. Putra, N.E.; LeeFlang, M.A.; Taheri, P.; Fratila-Apachitei, L.E.; Mol, J.M.C.; Zhou, J.; Zadpoor, A.A. Extrusion-based 3D printing of ex situ-alloyed highly biodegradable MRI-friendly porous iron-manganese scaffolds. *Acta Biomater.* **2021**, *134*, 774–790. [[CrossRef](#)] [[PubMed](#)]
26. Chen, Y.; Zeng, Z.; Li, Y.; Liu, Y.; Chen, Y.; Wu, Y.; Zhang, J.; Li, H.; Xu, R.; Wang, S. Glucose enhanced the oxidation performance of iron-manganese binary oxides: Structure and mechanism of removing tetracycline. *J. Colloid Interface Sci.* **2020**, *573*, 287–298. [[CrossRef](#)]
27. Hufenbach, J.; Kochta, F.; Wendrock, H.; Voß, A.; Giebler, L.; Oswald, S.; Pilz, S.; Kühn, U.; Lode, A.; Gelinsky, M. S and B microalloying of biodegradable Fe-30Mn-1C-Effects on microstructure, tensile properties, in vitro degradation and cytotoxicity. *Mater. Des.* **2018**, *142*, 22–35. [[CrossRef](#)]
28. Bagha, P.S.; Khakbiz, M.; Sheibani, S.; Hermawan, H. Design and characterization of nano and bimodal structured biodegradable Fe-Mn-Ag alloy with accelerated corrosion rate. *J. Alloys Compd.* **2018**, *767*, 955–965. [[CrossRef](#)]
29. Hong, D.; Chou, D.-T.; Velikokhatnyi, O.I.; Roy, A.; Lee, B.; Swink, I.; Issaev, I.; Kuhn, H.A.; Kumta, P.N. Binder-jetting 3D printing and alloy development of new biodegradable Fe-Mn-Ca/Mg alloys. *Acta Biomater.* **2016**, *45*, 375–386. [[CrossRef](#)]
30. Xu, Z.; Hodgson, M.A.; Cao, P. A comparative study of powder metallurgical (PM) and wrought Fe–Mn–Si alloys. *Mater. Sci. Eng. A* **2015**, *630*, 116–124. [[CrossRef](#)]

31. Liu, R.-Y.; He, R.-G.; Xu, L.-Q.; Guo, S.-F. Design of Fe–Mn–Ag alloys as potential candidates for biodegradable metals. *Acta Metall. Sin. English Lett.* **2018**, *31*, 584–590. [[CrossRef](#)]
32. Hufenbach, J.; Wendrock, H.; Kochta, F.; Kühn, U.; Gebert, A. Novel biodegradable Fe–Mn–CS alloy with superior mechanical and corrosion properties. *Mater. Lett.* **2017**, *186*, 330–333. [[CrossRef](#)]
33. Tang, Z.; Niu, J.; Huang, H.; Zhang, H.; Pei, J.; Ou, J.; Yuan, G. Potential biodegradable Zn–Cu binary alloys developed for cardiovascular implant applications. *J. Mech. Behav. Biomed. Mater.* **2017**, *72*, 182–191. [[CrossRef](#)] [[PubMed](#)]
34. Zhang, E.-L.; Fu, S.; Wang, R.-X.; Li, H.-X.; Liu, Y.; Ma, Z.-Q.; Liu, G.-K.; Zhu, C.-S.; Qin, G.-W.; Chen, D.-F. Role of Cu element in biomedical metal alloy design. *Rare Met.* **2019**, *38*, 476–494. [[CrossRef](#)]
35. Ingle, A.P.; Paralikar, P.; Shende, S.; Gupta, I.; Biswas, J.K.; da Silva Martins, L.H.; Rai, M. Copper in medicine: Perspectives and toxicity. In *Biomedical Applications of Metals*; Springer: Cham, Switzerland, 2018; pp. 95–112.
36. Roman, A.M.; Geantă, V.; Cimpoeșu, R.; Munteanu, C.; Lohan, N.M.; Zegan, G.; Cernei, E.R.; Ioniță, I.; Cimpoeșu, N.; Ioanid, N. In-vitro analysis of FeMn–Si smart biodegradable alloy. *Materials* **2022**, *15*, 568. [[CrossRef](#)] [[PubMed](#)]
37. Sivasankaran, S.; Ammar, H.R.; Al-Mufadi, F.A. Continuous hot-compaction behavior of nanostructured FeCrCuMnTi–(V, Zn) high-entropy alloys. *Mater. Manuf. Process.* **2022**, *37*, 1122–1131. [[CrossRef](#)]
38. Kuziora, P.; Wyszynska, M.; Polanski, M.; Bystrzycki, J. Why the ball to powder ratio (BPR) is insufficient for describing the mechanical ball milling process. *Int. J. Hydrogen Energy* **2014**, *39*, 9883–9887. [[CrossRef](#)]
39. Ammar, H.R.; Sivasankaran, S.; Alaboody, A.S. The influence of ball milling processing variables on the microstructure and compaction behavior of Fe–Mn–Cu alloys. *Mater. Sci.* **2021**, *39*, 410–429. [[CrossRef](#)]
40. Coşkun, S.; Öveçoğlu, M.L.; Özkal, B.; Tanoğlu, M. Characterization investigations during mechanical alloying and sintering of W–20 vol% SiC composites. *J. Alloys Compd.* **2010**, *492*, 576–584. [[CrossRef](#)]
41. Hermawan, H.; Alamdari, H.; Mantovani, D.; Dube, D. Iron–manganese: New class of metallic degradable biomaterials prepared by powder metallurgy. *Powder Metall.* **2008**, *51*, 38–45. [[CrossRef](#)]
42. Prashanth, M.; Karunanithi, R.; RasoolMohideen, S.; Sivasankaran, S. A comprehensive exploration on the development of nano Y2O3 dispersed in AA 7017 by mechanical alloying and hot-pressing technique. *Ceram. Int.* **2021**, *47*, 22924–22938. [[CrossRef](#)]
43. Shu, C.; Chen, K.; Yang, H.; Chen, M.; He, X. Effect of V and ball milling time on microstructure and thermal properties of CoCrCuFeNiVX by mechanical alloying. *Phys. B Condens. Matter* **2019**, *571*, 235–242. [[CrossRef](#)]
44. Goudarzi, P.; Moazami-Goudarzi, M.; Masoudi, A. Sintering, microstructure and properties of absorbable Fe–Mn–xCu alloys. *Mater. Chem. Phys.* **2022**, *287*, 126368. [[CrossRef](#)]
45. Bhadeshia, H.; Honeycombe, R. *Steels: Microstructure and Properties*; Butterworth-Heinemann: Oxford, UK, 2017; ISBN 0081002726.
46. Conti, M.C.; Mallia, B.; Sinagra, E.; Wismayer, P.S.; Buhagiar, J.; Vella, D. The effect of alloying elements on the properties of pressed and non-pressed biodegradable Fe–Mn–Ag powder metallurgy alloys. *Heliyon* **2019**, *5*, e02522. [[CrossRef](#)]
47. Bhadeshia, H.; Honeycombe, R. *Chapter 4—Solutes That Substitute for Iron*, 4th ed.; Butterworth-Heinemann: Oxford, UK, 2017; pp. 101–134, ISBN 978-0-08-100270-4.
48. Olejarz, A.; Huo, W.Y.; Zieliński, M.; Diduszko, R.; Wyszowska, E.; Kosińska, A.; Kalita, D.; Jóźwik, I.; Chmielewski, M.; Fang, F. Microstructure and mechanical properties of mechanically-alloyed CoCrFeNi high-entropy alloys using low ball-to-power ratio. *J. Alloys Compd.* **2022**, 168196. [[CrossRef](#)]
49. Tehrani, F.; Abbasi, M.H.; Golozar, M.A.; Panjepour, M. The effect of particle size of iron powder on α to γ transformation in the nanostructured high nitrogen Fe–Cr–Mn–Mo stainless steel produced by mechanical alloying. *Mater. Sci. Eng. A* **2011**, *528*, 3961–3966. [[CrossRef](#)]
50. Mendez, M.; Mancha, H.; Mendoza, G.; Escalante, J.I.; Cisneros, M.M.; Lopez, H.F. Structure of a Fe–Cr–Mn–Mo–N alloy processed by mechanical alloying. *Metall. Mater. Trans. A* **2002**, *33*, 3273–3278. [[CrossRef](#)]